AGU100 ADVANCING EARTH AND SPACE SCIENCE

Geophysical Research Letters

RESEARCH LETTER
10.1029/2019GL086081

Key Points:
- Four-dimensional quantification of a clearly resolved Kelvin-Helmholtz Instability event is observed with volumetric radar imaging
- The Richardson number is estimated to be much less than 0.25, using independent measurements
- The Froude number is estimated to be close to 1 (weak stratification) and a high buoyancy Reynolds number ~25,000 is estimated

Supporting Information:
- Supporting Information S1
- Movie S1

Correspondence to:
J. L. Chau,
chau@iap-kborn.de

Citation:
Chau, J. L., Urco, J. M., Avsarkisov, V., Vierinen, J. P., Latteck, R., Hall, C. M., & Tsutsumi, M. (2020). Four-dimensional quantification of Kelvin-Helmholtz instabilities in the polar summer mesosphere using volumetric radar imaging. *Geophysical Research Letters*, *47*, e2019GL086081. https://doi.org/10.1029/2019GL086081

Received 1 NOV 2019
Accepted 10 DEC 2019
Accepted article online 13 DEC 2019

Four-Dimensional Quantification of Kelvin-Helmholtz Instabilities in the Polar Summer Mesosphere Using Volumetric Radar Imaging

J. L. Chau[1], J. M. Urco[1], V. Avsarkisov[1], J. P. Vierinen[2], R. Latteck[1], C. M. Hall[3], and M. Tsutsumi[4]

[1]Leibniz Institute of Atmospheric Physics, University of Rostock, Kühlungsborn, Germany, [2]Department of Physics and Technology, UiT-The Arctic University of Norway, Tromsø, Norway, [3]Tromsø Geophysical Observatory, UiT-The Arctic University of Norway, Tromsø, Norway, [4]National Institute of Polar Research, Tokyo, Japan

Abstract We present and characterize in time and three spatial dimensions a Kelvin-Helmholtz Instability (KHI) event from polar mesospheric summer echoes (PMSE) observed with the Middle Atmosphere Alomar Radar System. We use a newly developed radar imaging mode, which observed PMSE intensity and line of sight velocity with high temporal and angular resolution. The identified KHI event occurs in a narrow layer of 2.4 km thickness centered at 85 km altitude, is elongated along north-south direction, presents separation between billows of ~8 km in the east-west direction, and its billow width is~3 km. The accompanying vertical gradients of the horizontal wind are between 35 and 45 m/s/km and vertical velocities inside the billows are ±12 m/s. Based on the estimated Richardson (<0.25), horizontal Froude (~0.8), and buoyancy Reynolds (~2.5×10^4) numbers, the observed event is a KHI that occurs under weak stratification and generates strong turbulence.

1. Introduction

In the mesosphere lower thermosphere (MLT) region, atmospheric instabilities account for wave dissipation, turbulence generation, and turbulent mixing. One of the most prominent MLT instabilities is the Kelvin-Helmholtz Instability (KHI) that occurs preferentially on strong shear of the horizontal wind due to gravity waves, tides, planetary waves, and mean flows. A necessary condition for KHI to occur is that the Richardson number (*Ri*) is less than 0.25 (e.g., Miles, 1961). These instabilities play an important role in the transport and deposition of energy and momentum (e.g., Fritts & Rastogi, 1985; Hecht, 2004; Hecht et al., 2007; Thorpe, 1973).

KHIs in the MLT have been inferred from a number of ground-based instruments (e.g., Hysell et al., 2012; Lehmacher et al., 2007) or characterized by using information from complementary instrumentation (e.g., Hecht, 2004; Li et al., 2005). For example, ripples observed in airglow imagers have been associated with KHIs and characterized with the aid of other supporting ground-based observations, for example, winds from specular meteor radars (SMRs), medium frequency radars, or lidars. In most cases, one or two dimensions of the events are not available. For example, in the case of airglow imagers, the vertical dimension is not. To overcome the relative large thickness of the airglow layer of a few kilometers, high-resolution ground- and balloon-based images of noctilucent clouds (NLCs) have been recently shown to be useful to study KHI with high spatial and temporal resolution (e.g., Baumgarten & Fritts, 2014; Fritts et al., 2014, 2019).

The relatively limited number of observations of KHIs in the mesosphere show a wide variety of spatial structures and alignments with respect to the background wind. These observations are being complemented with direct numerical simulations and large eddy simulations. The studies are particularly suitable for MLT cases, since they are characterized by high Reynolds numbers, that is, $\mathcal{O}(10^3)$ (e.g., Fritts et al., 2014; Marino et al., 2015). For example, the comparison of KHIs from NLC observations with numerical simulations indicate a turbulent viscosity much larger (5 to 40 times) than the true kinematic viscosity at the NLC altitude (e.g., Fritts et al., 2014).

In this work we quantify in four dimensions a KHI event observed in the polar mesosphere during summer. This unique observation has been made with the Middle Atmosphere Alomar Radar System (MAARSY)

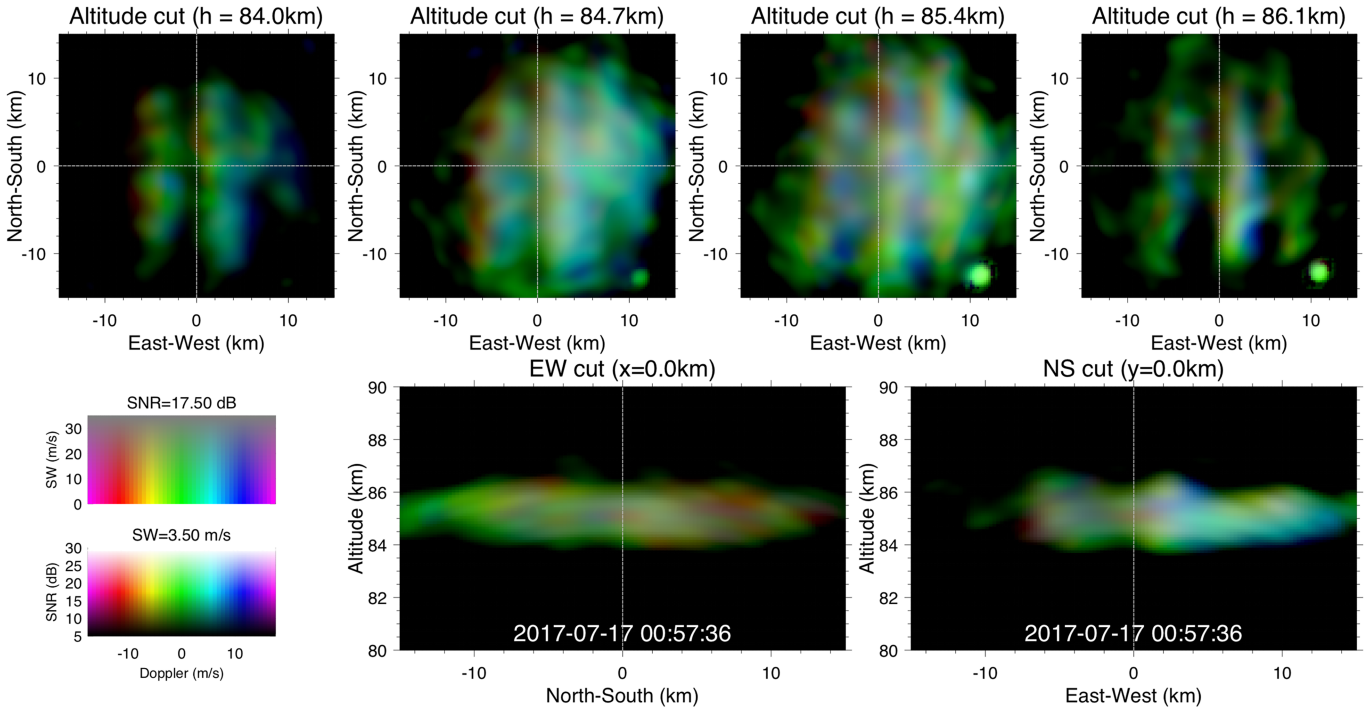

Figure 1. Two-dimensional cuts of a PMSE example obtained on 17 July 2017 at 00:54:43 UT: horizontal cuts at 83.8, 84.6, 85.4, and 86.2 km altitudes in the first row, respectively; and vertical east-west and north-south cuts at $x = 0$ and $y = 0$, respectively, in the second row. Doppler and signal-to-noise ratio (SNR) are color coded. SW in the legend stands for spectral width.

located in northern Norway. The clear quantification is possible due to an improved radar imaging of Polar Mesospheric Summer echoes (PMSEs) that utilizes a Multiple-Input Multiple-output (MIMO) approach developed by Urco et al. (2018). Currently there is general consensus that PMSEs are generated by atmospheric turbulence, but require the presence of free electrons and charged iced particles (e.g., Varney et al., 2011 and references therein) to increase the signal-to-noise ratio of the echoes sufficiently to make them observable with relatively low power atmospheric radars. Given that PMSE intensity depends on different parameters (turbulence, electron density, ice-particle density, electron density gradients, etc.), for this work we only rely in PMSE as tracer of the undergoing atmospheric dynamics.

The present paper is organized as follows. We first start with a brief description of the high-resolution four-dimensional radar observations and examples of what can be measured. Then we present the wind dynamics around the event under study, including a description of how the background winds are obtained. The specific dynamics during the event and the KHI observations from PMSE are shown in section 4. We end up with the quantification of the KHI event and the discussion of its parameters and atmospheric conditions.

2. High-Resolution Four-Dimensional Radar Observations

Mesosphere Stratosphere Troposhere radars are able to measure the neutral wind from Bragg scale ($\lambda/2$) atmospheric irregularities, where λ is the radar wavelength (e.g., Woodman & Guillén, 1974). Traditionally, they have provided atmospheric measurements with relative high temporal and vertical resolution over a particular region (e.g., Fukao et al., 2011; Lehmacher et al., 2007; Luce et al., 2012). Using phased arrays with electronic beam steering, modern atmospheric radars also provide horizontal information using a multibeam approach (e.g., Fukao et al., 1985; Latteck et al., 2012; Sato et al., 2014). Although the horizontal coverage is extended with this approach, the relatively long correlation time of atmospheric targets, the effects of a truncated antenna aperture, and the way electronic phasing is done (i.e., from pulse to pulse), the achieved angular and temporal resolutions have not been good enough to resolve atmospheric structures in the scales of kilometer- and minute-resolution, at least in the mesosphere (e.g., Stober et al., 2018).

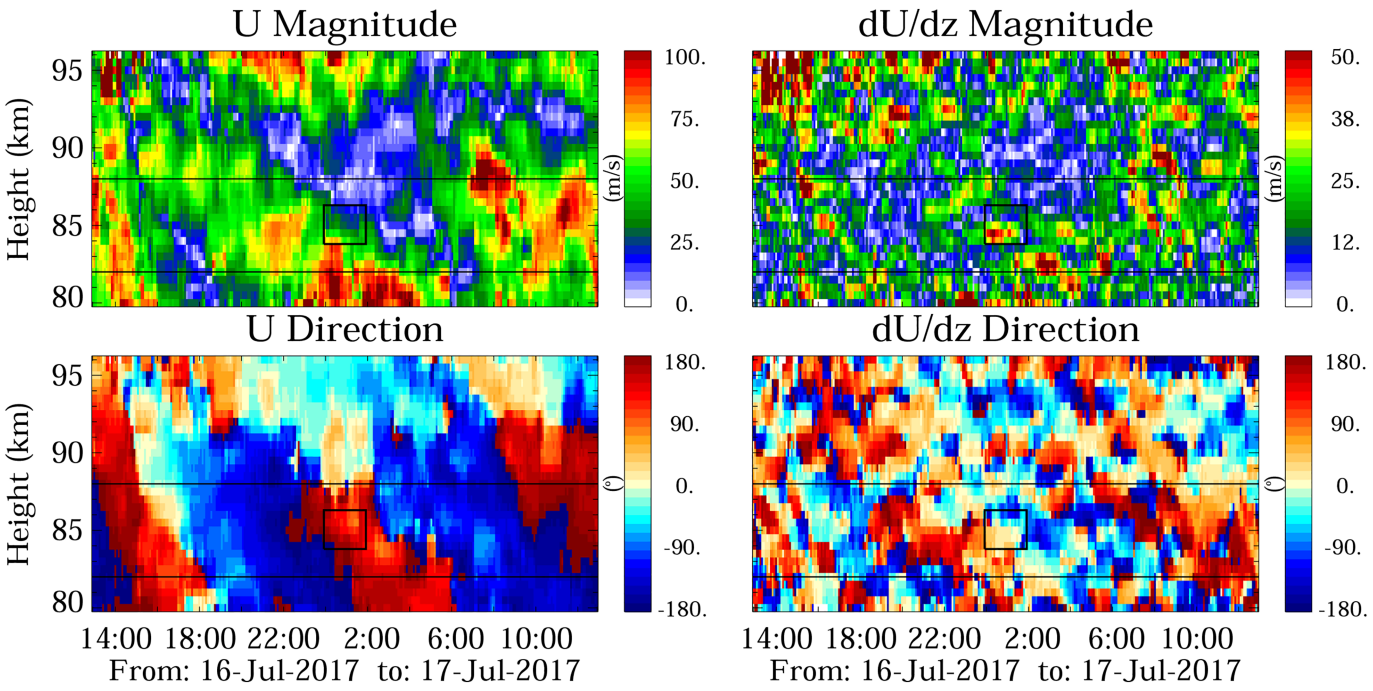

Figure 2. Mesospheric dynamics obtained with Tromsø and Andenes SMRs: (first column) Horizontal wind (U) magnitude and direction; (second column) Magnitude and direction of the vertical gradient of the horizontal wind (dU/dz). PMSE altitudes are in between horizontal lines. The rectangle indicates the time and altitude of a KHI event.

Besides the multibeam approach, in-beam radar imaging of ionospheric and atmospheric irregularities has been implemented. In the case of ionospheric irregularities, most of the implementations have been successful at separating spatial and temporal features (e.g., Hysell & Chau, 2006; Hysell et al., 2014). In the case of radar imaging of atmospheric irregularities, previous efforts have obtained results with varying degrees of success. In most cases, the procedures implemented (hardware and signal processing) were not good enough to resolve spatial scales smaller than the beam width (e.g., Chau & Woodman, 2001; Yu et al., 2001). Sommer and Chau (2016) using MAARSY with a wide beam transmitting beam and the Capon imaging technique, were able to identify PMSE structures smaller than the beam width on a statistical basis.

Recently, Urco et al. (2019) introduced a new radar imaging technique that makes use of a MIMO approach and a Maximum Entropy regularization technique. The MIMO approach has been implemented using time diversity, that is, three different one sixth of MAARSY's full array were interleaved in time. On reception 15 smaller sections called hexagons were used. This combination resulted in an effective 50% larger receiving aperture diameter than previous experiments, and 45 effective receiving channels. The achieved angular resolution is close to 0.6° (i.e., 0.9 km at 85 km), at least 6 times better than using the multibeam approach at MAARSY. More specific details of this implementation and other PMSE imaging examples can be found in Urco et al. (2019).

In Figure 1 we show an example of a volumetric PMSE radar image using six different two-dimensional cuts. There are four horizontal cuts at 83.8, 84.6, 85.4, and 86.2 km altitudes in the first row. The second row contains two vertical cuts, an east-west cut at $x = 0$ km, and a north-south cut at $y = 0$ km. These cuts were obtained on 17 July 2017 at 00:55:43 UT with 40 s of integration. The (x, y) coordinates are with respect to the center of the MAARSY array. Doppler line-of-sight velocity information is shown with color. Red represents velocities away from the radar (around −10 m/s) and blue velocities toward (around 10 m/s) the radar. Green represents velocities close to zero. The maximum velocities displayed are ±15 m/s. The intensity of the colors represents signal-to-noise ratio (SNR) on logarithmic scale, following the convention used in Urco et al. (2019).

Given that the obtained resolution is ~1 km in the horizontal direction at PMSE altitudes, most of the shown features are of atmospheric origin. In the case of the central altitudes, the PMSE strengths are at least two

orders of magnitude stronger than at the edges, allowing the observation of atmospheric dynamics associated to weaker echoes and smaller-scale dynamics.

From Figure 1, we can see ripples in all four horizontal cuts, elongated in the y direction. The dimensions of the billows associated to the ripples are 2.4 and 3.0 km in the z and x directions, respectively. Below we describe in more detail the spatial and temporal characteristics around this event and discuss its origin in terms of a KHI.

The temporal evolution of all these six two-dimensional cuts around the KHI event under study can be found in Movie S1 that is included in the supporting information. Note that these types of observations have been obtained during a larger special campaign in July 2017. A summary range-time-Doppler intensity plot of the 32 hr of measurements obtained during this campaign can be found in Urco et al. (2019), Figure 2.

3. Background Wind Dynamics

The occurrence of KHI is related to the background dynamics. Specifically Ri less than 0.25 is a necessary condition for KHI to occur, where Ri is a function of the horizontal wind, that is, $Ri = N^2/(dU/dz)^2$. Here N is the Brunt-Väisälä frequency, and $\mathrm{d}U/\mathrm{d}z$ is the vertical gradient of the horizontal wind (U).

Although PMSEs are good tracers of the wind dynamics (e.g., Rapp et al., 2008), measurements can only be obtained where there are PMSEs, and they are not present at all altitudes and times. To overcome this, we have obtained the mean mesospheric winds by using measurements from two closely located SMRs, specifically Tromsø (19.22°E, 69.58°N) and Andenes (16.04°E, 69.27°N). The combination of both systems allows us to have a higher meteor count and to obtain a zero-order Taylor expansion of the wind field (mean winds) with temporal and vertical sampling of 5 min and 500 m, using windows of 1 hr and 2 km, respectively (Chau et al., 2017). In order to observe the mean wind in a relatively localized region around the imaged radar volume, we have used only meteors that occur within 120 km horizontal radius around MAARSY.

Figure 2 shows the obtained background wind dynamics around the time of the KHI event of interest in this work. Specifically, we show the magnitude and direction of the horizontal wind (U), and the magnitude and direction of the vertical gradient of the horizontal wind ($\mathrm{d}U/\mathrm{d}z$), in the first and second columns, respectively. Eastward and northward directions are represented by 0° and 90°, respectively. PMSEs were observed between the horizontal black lines in all four figures. The black rectangles indicate the time and altitude of the KHI event below.

From a cursory look, the region within the rectangle is characterized by a strong westward wind at the bottom and weak wind tending northward at the top. During this time, $|U|$ is the smallest above this region. As expected, the associated $|\mathrm{d}U/\mathrm{d}z|$ is strong at the bottom of the rectangle. Note that there are other regions of strong $|\mathrm{d}U/\mathrm{d}z|$, many of them not occurring at PMSE altitudes.

4. Results

In this section we focus on the altitude dynamics around 17 July 2017 at 0055 UT event using SMR winds, as well as on the temporal and spatial evolution using high-resolution PMSE images, that is, around the KHI event of interest.

4.1. Altitude Profiles of Dynamics

In Figure 2 we showed the general dynamics around (a few hours) the event in question. To quantify better those dynamics, in Figure 3, we show the altitude profiles of the variables shown in Figure 2 in addition to the zonal (u) and meridional (v) components. The profiles are color coded in time, around ±60 min from the KHI event. The values at the time of the KHI event are shown with diamonds. In this plot, the horizontal lines indicate the altitude region of the KHI event.

The salient dynamical features at the central time of the event are as follows: (a) before the event u was stronger and v weaker at the bottom than after the event, (b) the effective $|\mathrm{d}U/\mathrm{d}z|$ was stronger before than after the event at the bottom, 45 m/s/km compared to 35 m/s/km, (c) at the event the strong wind at the bottom was westward, while at the top was to the north-west, (d) the direction of $\mathrm{d}U/\mathrm{d}z$ changes significantly from bottom to top. Therefore, the obtained $|\mathrm{d}U/\mathrm{d}z|$ values are strong and might produce KHI. Below we use these values to discuss the occurrence of a KHI event and its quantification.

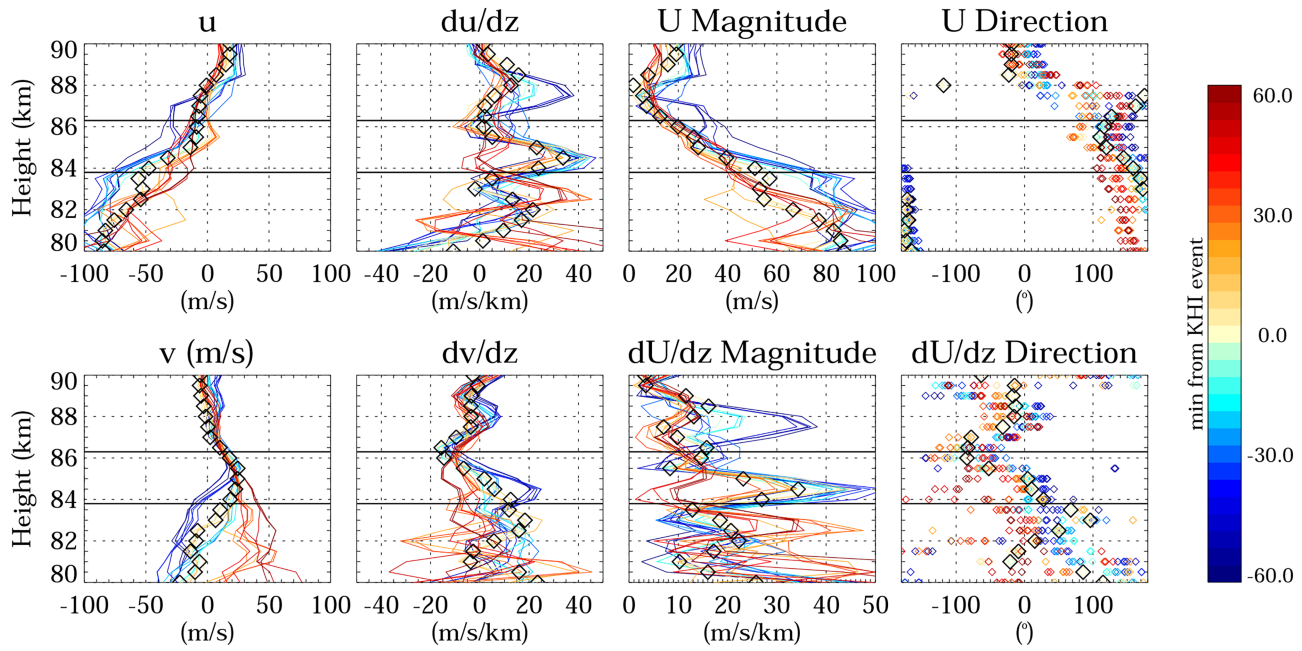

Figure 3. Altitude profiles of dynamics around the 17 July 2019 at 0055 UT over Andenes: u, du/dz, v, dv/dz, $|U|$, U direction, $|\mathrm{d}U/\mathrm{d}z|$, and $\mathrm{d}U/\mathrm{d}z$ direction, color coded in time (around ±60 min. Diamonds indicate the profile closer to the KHI event. Horizontal lines denote the bottom and top of the event.

4.2. Temporal Evolution of 2-D Cuts

Figure 4 shows the temporal evolution of horizontal cuts at $y = 0$ and $x = 0$, respectively. These cuts are shown for the same altitudes as the horizontal cuts presented in Figure 1, that is, 83.8, 84.6, 85.4, and 86.2 km, respectively. Doppler and SNR information are color coded with hue and intensity. This presentation is similar to those used in airglow imagers (so-called keograms), but resolved in a narrow altitude layer and with Doppler information included. The dotted lines represent the time and space cuts shown in Figure 1.

In all four altitude cuts there are organized ripples mainly drifting westward at ~30 m/s (i.e., 9 km in 5 min). Although we are combining Doppler and SNR information into one image, they are elongated in the north-south direction with a length of at least 20 km (see second column). The width of each of the ripples is less than 3 km (L_x) along the propagation direction, and the separation between them ~8 km (λ_x). In the transverse direction (i.e., NS), ~2-km structures (L_y) are observed, but not as clearly as the structures in the EW direction. At the altitude edges (i.e., 83.8 and 86.2 km), the ripples are more clearly observed than at the center altitudes where they coexist with PMSEs showing less organized structures. In the relative small observing area, up to six ripples are observed at the center altitudes.

5. Discussion

Taking into account the PMSE imaging information and the background dynamics, we can clearly see that the observed ripples are associated with a KHI event. Using an expected average buoyancy period of 400 s (e.g., Rapp et al., 2004) and the measured $S = |\mathrm{d}U/\mathrm{d}z|$ values (40 m/s/km; see Figure 3), the resulting Ri is ~0.15, that is, less than 0.25 that is necessary for sustained turbulence and thus occurrence of KHIs. However, $Ri < 0.25$ is not a sufficient condition for KHI occurrence. For example, according to Kunze et al. (1990) the KHI growth rate is proportional to $S - 2N$ over a large range of Ri, then small N would result on small Ri and also small growth rates. Our event is associated with a relative large S and is expected to be accompanied by a large growth rate (e.g., Hysell et al., 2012). However the estimation of growth rate required precised measurements of wind and temperature profiles (or N^2), that we do not have. Therefore, we shall discuss other characteristics that support our conclusion, that is, that the event is indeed a KHI.

In Figure 5 we show two dimensional cuts (xz and xy) at one particular time to quantify the KHI event better. Given that vertical resolution of the measured images (I_m) is only 450 m, and that there is the coexistence of other structures, in Figures 5b and 5e we show the fluctuations corresponding to Figures 5a and 5d. Such a fluctuating component (I^c_{wave}) has been obtained for each Doppler image c (i.e., red, green, and blue, see

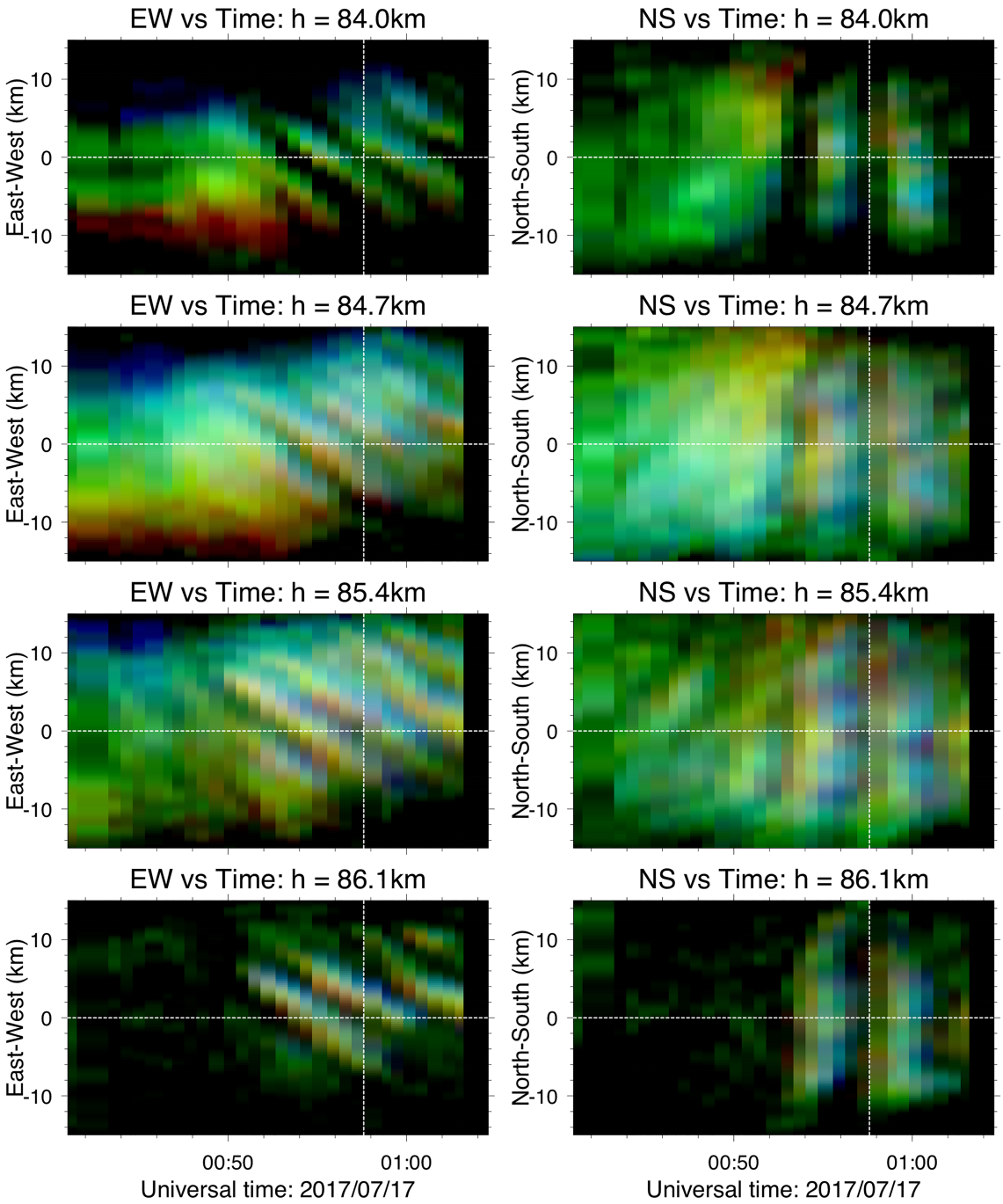

Figure 4. Temporal evolution of EW (left) and NS (right) cuts at $y = 0$ and $x = 0$, respectively. Doppler and SNR are color coded as before.

above) independently, by estimating a low-pass filtered version (I^c_{mean}) as follows:

$$I^c_{\text{wave}} = \frac{I^c_m - I_{\text{mean}}}{I^c_{\text{mean}}} \tag{1}$$

The low-pass filtered images have been obtained using a two-dimensional running mean smoothing with (20, 20) and (20,1) points for the xy and xz cuts, respectively. A similar procedure is used in airglow wave analysis (e.g., Garcia et al., 1997). The maximum values plotted for each of the Doppler images are ±25%.

The fluctuating components clearly show that the billows present upward velocities to the west and downward velocities to the east, in all three billows shown. The billow occurring at $x = -5$ km, is wider than

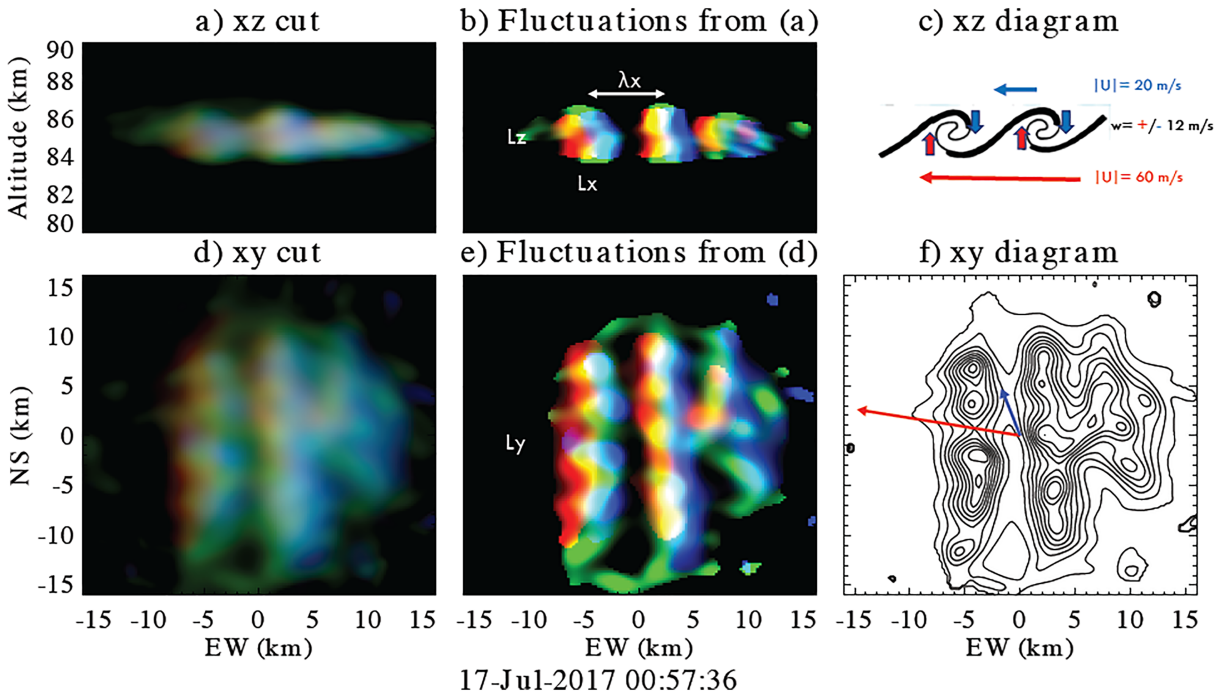

Figure 5. 2-D cuts of PMSEs images at 00:57:36 on 17 July 2017 for (a) *xz*, and (d) *xy*, similar to Figure 1. Their fluctuating components obtained using equation (1) are shown in panels (b) and (e), respectively. Sketches for the two cuts are shown in panels (c) and (f), respectively. The horizontal velocities at the bottom and top of the layers are indicated with red and blue thin arrows, respectively.

the other two billows and show "cat's-eye" structure (Figure 5b). In the NS direction, there are 2-km scale structures along the billows, that is, in the transverse direction to the propagation (Figure 5e). Perhaps these transverse structures are related to secondary billows reported in direct numerical simulations (e.g., Fritts et al., 2014), but our resolution is not high enough to resolve them better.

In Figures 5c and 5f we show simplified versions of the observed images, and to help with the interpretation we overplot the measured wind velocities, either from PMSE (vertical winds) or from the multistatic SMR (horizontal winds). Based on these results and sketches, the observed features of our KHI event are $L_x = 3$ km, $L_z = 2.4$ km (thickness in z), $\lambda_x = 8$ km, $U_z = 12$ m/s (i.e., the billow root-mean-square vertical velocity, half the maximum minus minimum vertical velocity), and propagation speed in the westward direction of 30 m/s. The propagation velocity is very similar to the mean background wind at the KHI altitudes, that is, implying a small phase velocity.

Additional evidence that supports the KHI interpretation of this event are the thickness to separation ratio of $L_z/\lambda_x \sim 0.3$ and the high vertical velocities accompanying the billows ($\pm$12 m/s). If we compare this ratio to numerical studies with high Reynolds numbers, the expected *Ri* is between 0.10 and 0.15 (e.g., Thorpe, 1973).

Using these length scales and vertical velocity, it is possible to apply the theory of stratified turbulence to explore some more details about the observed KHI event. By making the assumption that L_x, L_z, and U_z are the characteristic lengths and velocity scales of this event, and using the continuity equation, which has a nondivergent form in stratified turbulence (Davidson, 2013), we can obtain the following constraint:

$$\frac{L_x}{U_x} \sim \frac{L_z}{U_z}. \tag{2}$$

From (2) it is possible to derive the characteristic horizontal root-mean-square velocity: $U_x \sim U_z L_x/L_z = 15$ m/s.

A turbulent dissipation rate (ϵ) can be obtained from the definition of an integral length-scale $L_{\text{int}} \sim U^3/\epsilon$, which is an outer scale in homogeneous and isotropic turbulence. In the present case, the turbulent

dissipation rate is defined as

$$\epsilon = C_\epsilon \frac{U_x^3}{L_x} = 1.125 \text{ W/kg}, \tag{3}$$

here we assume that the constant $C_\epsilon = 1.0$ (e.g., Gargett, 1999, Figure 8). At this point, however, it should be noted that the turbulent dissipation rate obtained through equation (3) is a local value of ϵ for the observed KHI event. This value is comparable to the largest values measured with rockets near the polar summer mesopause (e.g., Lübken et al., 2002, Figure 2).

There is another scaling definition of L_z, namely $L_z = U_x/N$ (e.g., Billant & Chomaz, 2001). It indicates that the vertical scale of the turbulence is a thickness of the stratification level and it is defined exclusively by the dynamics of the stratified turbulent flow. With the usage of the new definition of L_z it is possible to obtain the local buoyancy frequency value, which is $N = U_x/L_z = 0.00625 \quad \text{s}^{-1}$. This corresponds to a buoyancy period of ~1,005 s, which is more than twice the value used above that represents average background conditions. This is not surprising since N is known to be highly variable in the mesosphere (e.g., Li et al., 2005). The new estimate of N is obtained locally and suggest that stratification effects inside the KHI event are negligibly small.

The theory of strongly stratified turbulence states that there are only two nondimensional parameters that exclusively define the turbulence regime in sheared and stratified flows (Brethouwer et al., 2007; Lindborg, 2006). These two parameters are the horizontal Froude number Fr and the buoyancy Reynolds number Re_b defined as

$$Fr = \frac{\epsilon}{NU_x^2} = \frac{U_x}{L_x N} \tag{4}$$

$$Re_b = \frac{\epsilon}{\nu N^2} = \frac{U_x^3}{\nu N^2 L_x} \tag{5}$$

where ν is the kinematic viscosity. In the present study, it is possible to calculate these two parameters for the KHI event with values of U_x, N, and L_x estimated above. Thus, we get $Fr = 0.8$ and $Re_b = 2.5 \times 10^4$. We have assumed $\nu = 1.15 \quad \text{m}^2/\text{s}$, which is expected in the polar summer mesosphere. The high horizontal Froude number $Fr > \mathcal{O}(10^{-2})$ indicates a weak stratification and that the observed turbulence event is generated through the KHI, while large Re_b suggests a wide inertial subrange of the kinetic and potential energy spectra of the present event.

The scaling analysis applied in the present study supports the observational result obtained with volumetric radar imaging without invoking a highly uncertain Miles-Howard criterion for turbulence existence, that is, $Ri < 0.25$ (e.g., Galperin et al., 2007). The local values of ϵ and N confirm the presence of very strong turbulence inside the detected structures, while the negligible degree of anisotropy indicates an absence of the stratification effects inside these structures.

6. Concluding Remarks

We have presented a high-resolution volumetric radar imaging measurement of KHI in the polar summer mesopause. The observation provides PMSE intensity and line-of-sight velocity measured as a function of time and three spatial dimensions. To our knowledge, this is the first spatially resolved measurement of mesospheric KHI observed with radar in four dimensions.

The event is composed of up to six elongated ripples in the NS direction, propagating to the west at ~30 m/s with separation between billows of ~8 km, a layer thickness of 2.4 km, and billow width of less than 3 km. The necessary conditions for being a KHI are satisfied, that is, $Ri < 0.25$ using expected buoyancy periods, measured $|\text{d}U/\text{d}z|$, scaling analysis, and comparisons with previous numerical simulations. Furthermore, based on the observed parameters, the event occurs with $Fr \sim 1$ and high Re_b, indicating conditions of weak stratification and a clear turbulent nature of the observed event, that is, KHI.

Although we have focused on just one KHI event, we are certain that many more events and not only KHI can be characterized with the type of PMSE volumetric imaging shown in this work. Given that not all the time one can separate easily the contributions of gravity waves and turbulence, one could quantify statistically such contributions by exploiting the multidimensional data with second-order statistics of the radial velocities, as it has been proposed by Vierinen et al. (2019).

The new volumetric radar imaging capability can augment existing lidar, radar, and airglow measurements used for studies of small-scale dynamics. As indicated by Fritts et al. (2014), these types of small-scale multi-dimensional observations coupled with modeling capabilities will enable a more complete quantification of small-scale dynamics and a better parameterization in large-scale general circulation atmospheric models.

Acknowledgments
This work was supported by the Deutsche Forschunggemeinschaft (DFG, German Research Foundation) under SPP 1788 (CoSIP)-CH1482/3-1. The authors thank useful comments from David Fritts and Raffaele Marino that help us interpret our observations. The wind data ("mmaria_par*.h5") and PMSE imaging data (under "Event01" directory) can be found both in HDF5 format at this site (ftp://ftp.iap-kborn.de/data-in-publications/ChauGRL2019). In the case of the PMSE Imaging data, each brightness file corresponds to ∼40 s integration and contains 129×129×101×16 points, representing x, y, z, and frequency bins. The corresponding metadata is contained in "metadata.h5."

References

Baumgarten, G., & Fritts, D. C. (2014). Quantifying Kelvin-Helmholtz Instability dynamics observed in noctilucent clouds: 1. Methods and observations. *Journal of Geophysical Research: Atmospheres*, *119*, 9324–9337. https://doi.org/10.1002/2014JD021832

Billant, P., & Chomaz, J. M. (2001). Self-similarity of strongly stratified inviscid flows. *Physics of Fluids*, *13*(6), 1645–1651. https://doi.org/10.1063/1.1369125

Brethouwer, G., Billant, P., Lindborg, E., & Chomaz, J. M. (2007). Scaling analysis and simulation of strongly stratified turbulent flows. *Journal of Fluid Mechanics*, *585*, 343–368. https://doi.org/10.1017/S0022112007006854

Chau, J. L., Stober, G., Hall, C. M., Tsutsumi, M., Laskar, F. I., & Hoffmann, P. (2017). Polar mesospheric horizontal divergence and relative vorticity measurements using multiple specular meteor radars. *Radio Science*, *52*, 811–828. https://doi.org/10.1002/2016RS006225

Chau, J. L., & Woodman, R. F. (2001). Three-dimensional coherent radar imaging at Jicamarca: Comparison of different inversion techniques. *Journal of Atmospheric and Solar-Terrestrial Physics*, *63*(2), 253–261. https://doi.org/10.1016/S1364-6826(00)00142-5

Davidson, P. A. (2013). *Turbulence in rotating, stratified and electrically conducting fluids*. Cambridge: Cambridge University Press.

Fritts, D. C., Baumgarten, G., Wan, K., Werne, J., & Lund, T. (2014). Quantifying Kelvin-Helmholtz Instability dynamics observed in noctilucent clouds: 2. Modeling and interpretation of observations. *Journal of Geophysical Research: Atmospheres*, *119*, 9359–9375. https://doi.org/10.1002/2014JD021833

Fritts, D. C., Miller, A. D., Kjellstrand, C. B., Geach, C., Williams, B. P., Kaifler, B., et al. (2019). PMC Turbo: Studying gravity wave and instability dynamics in the summer mesosphere using polar mesospheric cloud imaging and profiling from a stratospheric balloon. *Journal of Geophysical Research: Atmospheres*, *124*, 6423–6443. https://doi.org/10.1029/2019JD030298

Fritts, D. C., & Rastogi, P. K. (1985). Convective and dynamical instabilities due to gravity wave motions in the lower and middle atmosphere: Theory and observations. *Radio Science*, *20*(6), 1247–1277. https://doi.org/10.1029/RS020i006p01247

Fukao, S., Luce, H., Mega, T., & Yamamoto, M. K. (2011). Extensive studies of large-amplitude Kelvin–Helmholtz billows in the lower atmosphere with VHF middle and upper atmosphere radar. *Quarterly Journal of the Royal Meteorological Society*, *137*(657), 1019–1041. https://doi.org/10.1002/qj.807

Fukao, S., Sato, T., Tsuda, T., Kato, S., Wakasugi, K., & Makihira, T. (1985). The MU radar with an active phased array system, 1. Antenna and power amplifiers. *Radio Science*, *20*(6), 1155–1168. https://doi.org/10.1029/RS020i006p01155

Galperin, B., Sukoriansky, S., & Anderson, P. S. (2007). On the critical Richardson number in stably stratified turbulence. *Atmospheric Science Letters*, *8*, 65–69. https://doi.org/10.1002/asl.153

Garcia, F. J., Taylor, M. J., & Kelley, M. C. (1997). Two-dimensional spectral analysis of mesospheric airglow image data. *Applied Optics*, *36*(29), 7374–7385. https://doi.org/10.1364/AO.36.007374

Gargett, A. E. (1999). Velcro measurement of turbulenc kinetic energy dissipation rate ϵ. *Journal of Atmospheric and Oceanic Technology*, *16*(12), 1973–1993. https://doi.org/10.1175/1520-0426(1999)016<1973:VMOTKE>2.0.CO;2

Hecht, J. H. (2004). Instability layers and airglow imaging. *Reviews of Geophysics*, *42*, RG1001. https://doi.org/10.1029/2003RG000131

Hecht, J. H., Liu, A. Z., Walterscheid, R. L., Franke, S. J., Rudy, R. J., Taylor, M. J., & Pautet, P. D. (2007). Characteristics of short-period wavelike features near 87 km altitude from airglow and lidar observations over Maui. *Journal of Geophysical Research*, *112*, D16101. https://doi.org/10.1029/2006JD008148

Hysell, D. L., Aveiro, H. C., & Chau, J. L. (2014). Ionospheric irregularities, *Modeling the ionosphere–thermosphere system* J. Huba, R. Schunk, & G. Khazanov Eds., https://doi.org/10.1002/9781118704417.ch18

Hysell, D. L., & Chau, J. L. (2006). Optimal aperture synthesis radar imaging. *Radio Science*, *41*, RS2003. https://doi.org/10.1029/2005RS003383

Hysell, D. L., Nossa, E., Larsen, M. F., Munro, J., Smith, S., Sulzer, M. P., & González, S. A. (2012). Dynamic instability in the lower thermosphere inferred from irregular sporadic E layers. *Journal of Geophysical Research*, *117*, A08305. https://doi.org/10.1029/2012JA017910

Kunze, E., Williams III, A. J., & Briscoe, M. G. (1990). Observations of shear and vertical stability from a neutrally buoyant float. *Journal of Geophysical Research*, *95*(C10), 18,127–18,142. https://doi.org/10.1029/JC095iC10p18127

Latteck, R., Singer, W., Rapp, M., Vandepeer, B., Renkwitz, T., Zecha, M., & Stober, G. (2012). MAARSY: The new MST radar on Andøya—System description and first results. *Radio Science*, *47*, RS1006. https://doi.org/10.1029/2011RS004775

Lehmacher, G., Guo, L., Kudeki, E., Reyes, P., Akgiray, A., & Chau, J. (2007). High-resolution observations of mesospheric layers with the Jicamarca VHF radar. *Advances in Space Research*, *40*(6), 734–743. https://doi.org/10.1016/j.asr.2007.05.059

Li, F., Liu, A. Z., & Swenson, G. R. (2005). Characteristics of instabilities in the mesopause region over Maui, Hawaii. *Journal of Geophysical Research*, *110*, D09S12. https://doi.org/10.1029/2004JD005097

Li, F., Liu, A. Z., Swenson, G. R., Hecht, J. H., & Robinson, W. A. (2005). Observations of gravity wave breakdown into ripples associated with dynamical instabilities. *Journal of Geophysical Research*, *110*, D09S11. https://doi.org/10.1029/2004JD004849

Lindborg, E. (2006). The energy cascade in a strongly stratified fluid. *Journal of Fluid Mechanics*, *550*, 207–242. https://doi.org/10.1017/S0022112005008128

Lübken, F. J., Rapp, M., & Hoffmann, P. (2002). Neutral air turbulence and temperatures in the vicinity of polar mesosphere summer echoes. *Journal of Geophysical Research*, *107*(D15), 4273. https://doi.org/10.1029/2001JD000915

Luce, H., Nishi, N., Caccia, J. L., Fukao, S., Yamamoto, M. K., Mega, T., et al. (2012). Kelvin-Helmholtz billows generated at a cirrus cloud base within a tropopause fold/upper-level frontal system. *Geophysical Research Letters*, *39*, L04807. https://doi.org/10.1029/2011GL050120

Marino, R., Rosenberg, D., Herbert, C., & Pouquet, A. (2015). Interplay of waves and eddies in rotating stratified turbulence and the link with kinetic-potential energy partition. *Europhysics Letters*, *112*(4), 49001. https://doi.org/10.1209/0295-5075/112/49001

Miles, J. W. (1961). On the stability of heterogeneous shear flows. *Journal of Fluid Mechanics*, *10*(4), 496–508. https://doi.org/10.1017/S0022112061000305

Rapp, M., Strelnikova, I., Latteck, R., Hoffmann, P., Hoppe, U. P., Häggström, I., & Rietveld, M. (2008). Polar Mesosphere Summer Echoes (PMSE) studied at Bragg wavelengths of 2.8 m, 67 cm, and 16 cm. *Journal of Atmospheric and Solar Terrestrial Physics*, *70*, 947–961. https://doi.org/10.1016/j.jastp.2007.11.005

Rapp, M., Strelnikov, B., Müllemann, A., Lübken, F. J., & Fritts, D. C. (2004). Turbulence measurements and implications for gravity wave dissipation during the MaCWAVE/MIDAS rocket program. *Geophysical Research Letters*, *31*, L24S07. https://doi.org/10.1029/2003GL019325

Sato, K., Tsutsumi, M., Sato, T., Nakamura, T., Saito, A., Tomikawa, Y., et al. (2014). Program of the Antarctic Syowa MST/IS radar (PANSY). *Journal of Atmospheric and Solar-Terrestrial Physics*, *118*, 2–15. https://doi.org/10.1016/j.jastp.2013.08.022

Sommer, S., & Chau, J. L. (2016). Patches of polar mesospheric summer echoes characterized from radar imaging observations with MAARSY. *Annales Geophysicae*, *34*(12), 1231–1241. https://doi.org/10.5194/angeo-34-1231-2016

Stober, G., Sommer, S., Schult, C., Latteck, R., & Chau, J. L. (2018). Observation of Kelvin–Helmholtz instabilities and gravity waves in the summer mesopause above Andenes in Northern Norway. *Atmospheric Chemistry and Physics*, *18*(9), 6721–6732. https://doi.org/10.5194/acp-18-6721-2018

Thorpe, S. A. (1973). Experiments on instability and turbulence in a stratified shear flow. *Journal of Fluid Mechanics*, *61*(4), 731–751. https://doi.org/10.1017/S0022112073000911

Urco, J. M., Chau, J. L., Milla, M. A., Vierinen, J. P., & Weber, T. (2018). Coherent MIMO to improve aperture synthesis radar imaging of field-aligned irregularities: First results at Jicamarca. *IEEE Transactions on Geoscience and Remote Sensing*, *PP*(99), 1–11. https://doi.org/10.1109/TGRS.2017.2788425

Urco, J. M., Chau, J. L., Weber, T., & Latteck, R. (2019). Enhancing the spatio-temporal features of polar mesosphere summer echoes using coherent MIMO and radar imaging at MAARSY. *Atmospheric Measurement Techniques*, *12*, 955–969. https://doi.org/10.5194/amt-12-955-2019

Varney, R. H., Kelley, M. C., Nicolls, M. J., Heinselman, C. J., & Collins, R. L. (2011). The electron density dependence of polar mesospheric summer echoes. *Journal of Atmospheric and Solar-Terrestrial Physics*, *73*, 2153–2165. https://doi.org/10.1016/j.jastp.2010.07.020

Vierinen, J., Chau, J. L., Charuvil, H., Urco, J. M., Clahsen, M., Avsarkisov, V., et al. (2019). Observing mesospheric turbulence with specular meteor radars: A novel method for estimating second-order statistics of wind velocity. *Earth and Space Science*, *6*(7), 1171–1195. https://doi.org/10.1029/2019EA000570

Woodman, R. F., & Guillén, A. (1974). Radar observations of winds and turbulence in the stratosphere and mesosphere. *Journal of the Atmospheric Sciences*, *31*(2), 493–505.

Yu, T. Y., Palmer, R. D., & Chilson, P. B. (2001). An investigation of scattering mechanisms and dynamics in PMSE using coherent radar imaging. *Journal of Atmospheric and Solar-Terrestrial Physics*, *63*(17), 1797–1810. https://doi.org/10.1016/S1364-6826(01)00058-X